Vacuum 230 (2024) 113676

Contents lists available at ScienceDirect

Vacuum

journal homepage: www.elsevier.com/locate/vacuum

The migration behaviour of strontium co-implanted with helium into SiC at room temperature and annealed at temperatures above 1000 °C

T.T. Hlatshwayo [a,*], T.F. Mokgadi [a], A. Sohatsky [b], Z.A.Y. Abdalla [a], V.A. Skuratov [b,c,d], E.G. Njoroge [a,e], M. Mlambo [f]

[a] Physics Department, University of Pretoria, Private Bag X20, 0028 Hatfield, South Africa
[b] Joint Institute for Nuclear Research, Dubna, Russia
[c] National Research Nuclear University MEPhI, Moscow, Russia
[d] Dubna State University, Dubna, Moscow region, Russia
[e] ENGAGE, University of Pretoria, Private Bag X20, 0028 Hatfield, South Africa
[f] Nanotechnology Innovation Centre, Health Platform, Advanced Materials Division, Mintek, Randburg, South Africa

ARTICLE INFO

Handling Editor: Prof. L.G. Hultman

Keywords:
Sr precipitates
Cavities
Annealing
Helium
Epitaxial regrowth

ABSTRACT

The study investigated the migration behaviour of Sr implanted into SiC in the presence of helium (He). Sr ions were implanted into polycrystalline SiC samples (Sr-SiC) at room temperature (RT), and co-implanted with He ions also at RT (Sr + He-SiC). The samples were then annealed isochronally at 1100 °C, 1200 °C, and 1300 °C for 5 h. Transmission electron microscopy (TEM) and Rutherford backscattering spectrometry (RBS) were used to characterize both as-implanted and annealed annealed samples. Sr implantation induced amorphization of SiC, while co-implantation with He led to the formation of He nano-bubbles within the amorphous SiC matrix. During annealing, Sr migrated towards the surface, resulting in loss of Sr, cavity formation, and formation of Sr precipitates in the Sr-SiC samples. In Sr + He-SiC samples, He-induced cavities formed around the projected range of Sr, inhibiting epitaxial regrowth of SiC. As a result, the Sr distribution became concentrated around these He cavities, with Sr trapped both in front and behind them. The enhanced migration of Sr in annealed Sr + He-SiC is attributed to the slower recrystallization of the damaged SiC layer, the presence of larger He-induced cavities, and increased surface roughness. These findings provide insights into Sr migration the mechanisms in SiC, relevant for enhancing the safety of nuclear fuels.

1. Introduction

In modern fission nuclear reactors, silicon carbide (SiC) plays a crucial role as the primary barrier material for fission products within tri-structural isotropic (TRISO) fuel particles [1,2]. TRISO particles are highly effective in retaining most fission products, though they exhibit lower retention capabilities for specific nuclides such as ^{90}Sr, ^{110m}Ag, ^{134}I, ^{131}Cs, ^{137}Cs, ^{88}Kr, and ^{133}Xe [3,4]. The release of these fission products from TRISO fuel particles can pose significant radiological hazards. For instance, ^{90}Sr, a medium-lived fission product, can be absorbed by the body similar to calcium and poses potential health risks. Therefore, understanding the migration behaviour of strontium in SiC under various conditions that mimic fission reactor environments has been investigated [4–10]. These studies have explored SiC under high thermal conditions [5,6], the impact of radiation damage [4,7,8], swift heavy ion (SHI) irradiation [9], and the influence of silver (Ag) on the migration of Sr in SiC [10]. However, in fission nuclear reactors, SiC is subjected to diverse forms of irradiation, such as ions of varying energies and neutrons, at high temperatures. This occurs in the presence of helium (He), which is generated from actinide radioactive decay and nuclear transmutations [11]. The low solubility of He in SiC results in He atoms becoming trapped in helium-vacancy clusters and subsequently forming bubbles [12,13]. While some studies have concentrated on the impact of He on microstructural evolution [14–19], others have explored its effects on the migration of fission products in SiC [20–25]. The results of these studies indicate that the migration of co-implanted species is governed by their trapping in He induced cavities. Understanding how helium affects the migration and retention of fission products in SiC across the temperature ranges encountered during nuclear reactor operations and accidental conditions is crucial for ensuring

* Corresponding author.
E-mail address: thulani.hlatshwayo@up.ac.za (T.T. Hlatshwayo).

https://doi.org/10.1016/j.vacuum.2024.113676
Received 19 June 2024; Received in revised form 19 September 2024; Accepted 22 September 2024
Available online 24 September 2024

the safe operation of nuclear fission reactors, particularly with regard to TRISO fuel particles.

This study builds upon our prior work [23] on the structural evolution of SiC co-implanted with Sr and He at room temperature, simulating a highly defective SiC structure under nuclear fission irradiation. The samples were annealed at operational (1000 °C) and potential accidental temperatures (1100–1300 °C). We investigated the structural evolution of SiC at operational temperature, observing the formation of helium bubbles, surface swelling, and complete amorphization in the implanted region. Sr-only implanted SiC samples fully recovered after annealing at 1200 °C for 5 h. However, Sr and He co-implanted SiC samples experienced graphitization and limited recrystallization. Short-range order improved at 1000 °C and 1100 °C for the co-implanted system, while at 1200 °C and 1300 °C, chemical disorder increased, along with the number of defects in the C-C lattice site. He-induced craters formed on the surface during annealing due to surface exfoliation and He out-diffusion. Sr migration in the co-implanted system exhibited diffusion towards the surface, followed by some Sr loss and trapping around the projected range of implantation. Chemical disorder, Relative Raman Intensity (RRI) or total disorder, and the ID/IG ratio revealed deviations from the expected trend at 1200 °C and 1300 °C, indicating the formation of larger defects at these temperatures. This current study aims to investigate Sr migration and trapping behaviour in the co-implanted system above the reactor operational temperature and compare it with the Sr-only system. Chemical disorder, Relative Raman Intensity (RRI) or total disorder, and the ID/IG ratio revealed deviations from the expected trend at 1200 °C and 1300 °C, indicating the formation of larger defects at these temperatures. Consequently, our TEM measurements focus on these two temperatures.

To achieve this objective, Sr ions with an energy of 360 keV were implanted into SiC at room temperature Some of the Sr implanted SiC samples were then implanted with He ions also at room temperature. Both the individually implanted and co-implanted SiC samples were then subjected to isochronal annealing at temperatures above 1000 °C. The findings from this study will offer valuable insights into the behaviour of strontium in highly defective SiC in the presence of helium under laboratory conditions that simulate environments similar to those found in fission nuclear reactors. These insights will be pivotal in enhancing the safety standards of modern fission nuclear reactors.

2. Experimental procedure

Polycrystalline SiC wafers, composed mainly of 3C-SiC with some traces of 6H-SiC [10] from Valley Design Corporation were employed in this study. Sr ions, with an energy of 360 keV, were implanted into SiC at room temperature (RT) to a fluence of 2×10^{16} cm^{-2} (Sr-SiC) at Friedrich Schiller University in Jena, Germany. Subsequently, some Sr-SiC samples were co-implanted with 21.5 keV He ions to a fluence of 1×10^{17} cm^{-2} at RT (Sr + He-SiC). The helium implantation was done at the tandem accelerator mass spectrometry (TAMS) facilities of iThemba LABS in Gauteng, South Africa. Given that SiC in the fission nuclear reactors undergoes severe ion and neutron irradiation, resulting in a highly damaged structure, the implantation was conducted at RT to generate a highly defective structure.

The as-implanted Sr-SiC and Sr + He-SiC samples were isochronally annealed under 10^{-5} Pa vacuum for 5 h at temperatures ranging from 1100 to 1300 °C in steps of 100 °C, using the computer-controlled *Webb 77* graphite furnace. Characterization of the samples before and after annealing was conducted using transmission electron microscopy (TEM) and Rutherford backscattering spectrometry (RBS).

TEM lamellae of the as-implanted and annealed samples were prepared using the *FEL Helios Nanolab 650* focused ion beam (FIB). Lamellae thinning was achieved by successive 30 keV and 5 keV gallium (Ga) ion beams, with final polishing performed using 2 keV and 5 eV beams to produce near-damage-free TEM lamellae. Scanning TEM (STEM) equipped with high-angle angle dark field (HAADF) and energy-dispersive X-ray spectroscopy (EDS) detectors were employed to investigate the distribution of Sr atoms. TEM analysis before and after annealing was performed at the Joint Institute for Nuclear Research (JINR) in Dubna, using a *Thermoscientific Talos F200i* field emission transmission electron microscope operating at 200 kV. To obtain the Sr depth distribution profiles, Sr-Kα emission maps were measured from the cross-sectional samples. The lines of the measured profiles were perpendicular to the edge of the sample, and the intensities collected from large areas parallel to the edge were averaged. The positions of the sample edges corresponding to the surfaces in the Sr-Kα profiles were determined by aligning the profiles obtained from the maps for Sr-Kα with the intensity profiles of the bright field (BF) STEM images where the edge positions were clearly identified.

Sr migration was also monitored using RBS analysis performed at the tandem accelerator in iThemba LABS. The RBS measurements were performed at RT using $^{4}He^{+}$ beam of 2.0 MeV. The beam was maintained at a current of approximately 500 pA, and charge of 0.5 μC was collected per measurement. The scattered particles were detected using a solid-state detector at a backscattering angle of 150°. The RBS spectra were converted from energy-channel to depth using energy loss data by Ziegler [26] and the SiC density of 3.21 gcm^{-3}.

Using the stopping and range of ions in matter (SRIM 2013) [26], simulations were conducted to firstly determine the energy of Sr and He ions to be implanted so that they overlap and secondly to determine the relative atomic density of Sr and He implanted into SiC and their displacement per atom (dpa) as a function of depth. The detailed calculations in full damage cascades mode, with SiC density of 3.21 gcm^{-3} and displacement energies (E_d) of 35 eV and 20 eV for Si and C, respectively were used during simulations [27]. The fluence was converted to dpa as described in Ref. [28].

The simulated Sr and He results presented in Ref. [23] and also overlayed in Fig. 1 indicate that the implanted profiles of Sr and He were Gaussian with maximum relative atomic densities of 2.26 at% and 12 at % at depths of 140 nm and 150 nm below the surface, respectively. The maximum lattice damage of 2.60 dpa and 1.93 dpa were retained at a depth of approximately 110 nm and 130 nm for Sr and He, respectively. The total maximum lattice damage was found to be about 4.40 dpa at a depth of 110 nm below the surface.

3. Results

Fig. 1 shows the bright field (BF) TEM cross-sectional micrographs of the SiC samples individually implanted with Sr ions (Sr-SiC) (a) and successively implanted with Sr and He ions (Sr + He-SiC) (b) and selected area diffraction (SAD) patterns from the different parts of Sr-SiC sample (c). Implantation of Sr resulted in the amorphization of SiC up to a depth of approximately 270 nm from the surface, as indicated by SAD patterns showing a diffuse ring compared to the sharp spots observed in the SAD patterns of the SiC substrate (c). This diffuse ring signifies the loss of long-range ordering in the implanted SiC layer. Co-implantation with He further extended the amorphized layer to about 310 nm. The latter was due to further swelling caused by the formation of He nanobubbles at a depth 75–150 nm below the surface (indicated by arrows and vertical lines in Fig. 1 (b)). The implanted Sr and He profiles are embedded within the amorphous SiC layer in both Sr-SiC and Sr + He-SiC samples-Fig. 1(a) and (b). The amorphization of SiC after the implantation of Sr and He was anticipated, considering that the implantation energies and fluences of both Sr and He caused damage above the critical amorphization displacement per atom (dpa) threshold of SiC (0.3 dpa) [29].

Fig. 2(a)and (b) present the RBS spectra of Sr-SiC before and after isochronal annealing, along with their respective Sr depth profiles. Fig. 2 (c) illustrates the Sr retained ratio, full width at half maximum (FWHM), and peak position as functions of annealing temperature. The arrows in the RBS spectra indicate the surface position in channel numbers of C, Si, and Sr.

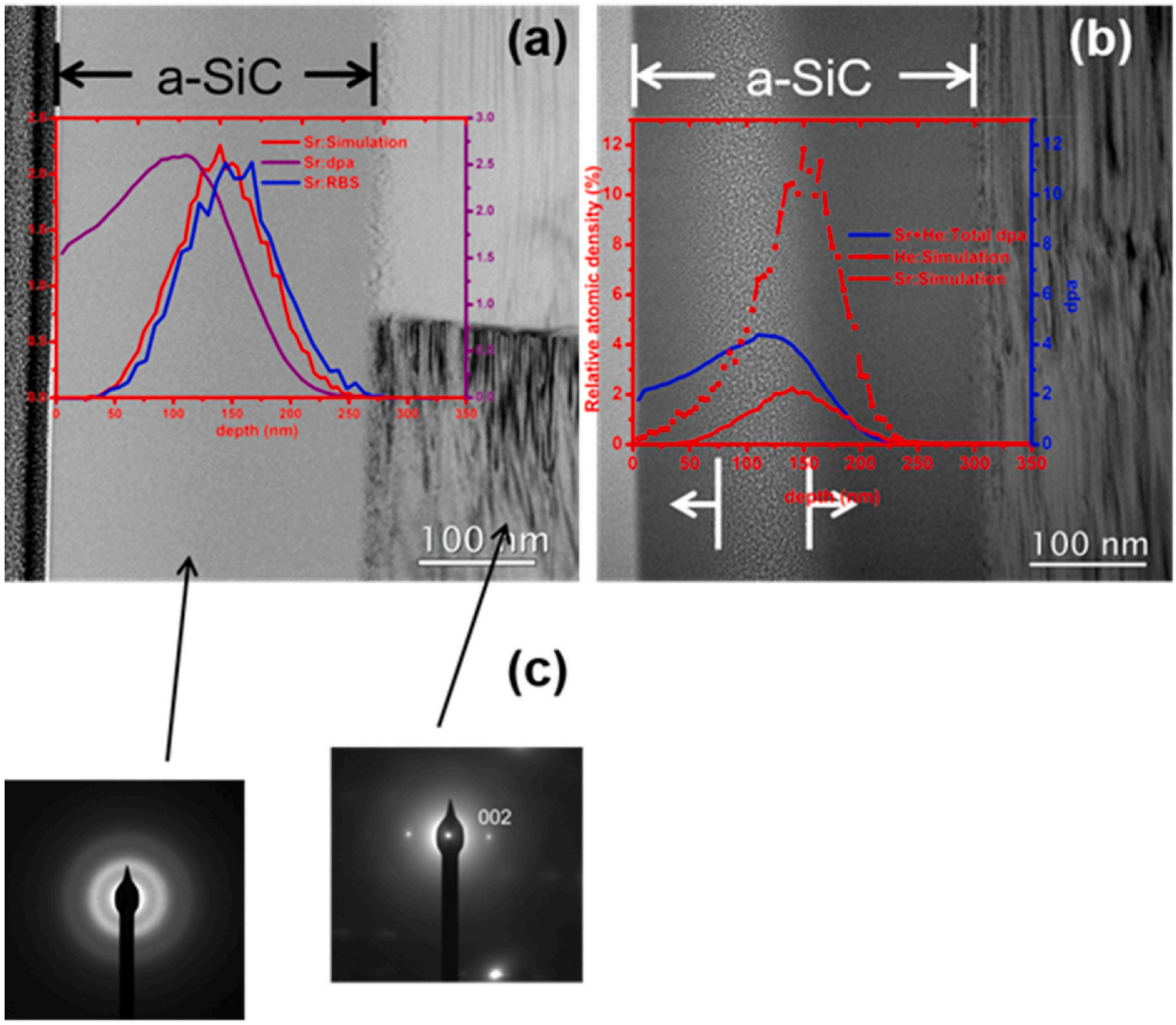

Fig. 1. BF TEM cross-sectional micrographs of Sr-SiC (a), Sr + He-SiC (b) and (c) SAD patterns from different parts of the Sr-SiC sample (indicated with arrows). Both micrographs are overlayed with their respective SRIM simulated and RBS results. Double arrows indicate the amorphous SiC (a-SiC) layer from the surface to the amorphous-crystalline (a–c) interface.

The retained ratio of Sr was calculated as the ratio of the total integrated counts of the Sr profile in the annealed samples to the as-implanted one. It is important to note that in this study, new as-implanted samples were annealed at different temperatures for the same duration, ensuring they all had the same initial defect level. Annealing at 1100 °C and 1200 °C caused broadening, coupled with the loss of Sr from the surface. This was expected as migration of Sr accompanied by loss has already been reported for the Sr-SiC sample annealed at 1000 °C [23]. Approximately 34 % and 41 % of Sr was lost in the Sr-SiC samples annealed at 1100 and 1200 °C, respectively. Moreover, the Sr profile of the Sr-SiC annealed at 1200 °C became bimodal, with a minimum around the projected range. These results indicate migration governed by the diffusion of Sr towards the surface, resulting in loss from the surface. A significant loss of approximately 63 % Sr was observed in the Sr-SiC sample annealed at 1300 °C. This loss was accompanied by a drastic shift of the Sr peak position towards the surface. A robust migration of Sr towards the surface after annealing the Sr-SiC at 1000 °C was noted in Ref. [23]. This behaviour is attributed to the amorphization of the surface region during implantation, a phenomenon that was also observed in Sr-implanted 6H-SiC at room temperature (amorphized 6H-SiC) and subsequently annealed at 1000 °C [7]. The observed migration is facilitated by epitaxial recrystallization from the amorphous-crystalline (a-c) interface, enhancing the movement of defects towards the surface.

The Sr loss follows a recovery process observed in the isochronally annealed Sr-SiC samples, as reported in our previous study [23]. The substantial loss at 1300 °C, accompanied by a drastic peak shift, is not solely driven by the recovery process but is also influenced by the growth of numerous small crystals on the surface, as reported in Ref. [23]. The appearance of these crystals coincides with the emergence of pores, serving as out-migration paths for Sr at 1300 °C, leading to additional Sr loss [23].

Fig. 2 (a') and (b') present the RBS spectra and Sr RBS depth profiles of the Sr + He-SiC samples before and after annealing, respectively. Their corresponding Sr retained ratio as a function of annealing temperature is shown in Fig. 2 (c'). Similar to the Sr-SiC samples, the new as-implanted Sr + He-SiC samples underwent isochronal annealing at various temperatures.

Annealing the Sr + He-SiC sample at 1100 °C resulted in the migration of Sr towards the surface, accompanied by a significant loss of approximately 70 % of implanted Sr. This migration also led to the segregation of Sr atoms resulting in a double-peaked retained Sr profile. The first peak, located before the projected range or closer to the surface (around 60 nm), and the second peak beyond the projected range (around 208 nm) with a minimum around the projected range were observed. These results are consistent with our previous findings for Sr + He-SiC sample annealed at 1000 °C [23]. Similar migration patterns characterized by loss and segregation were observed in the Sr + He-SiC

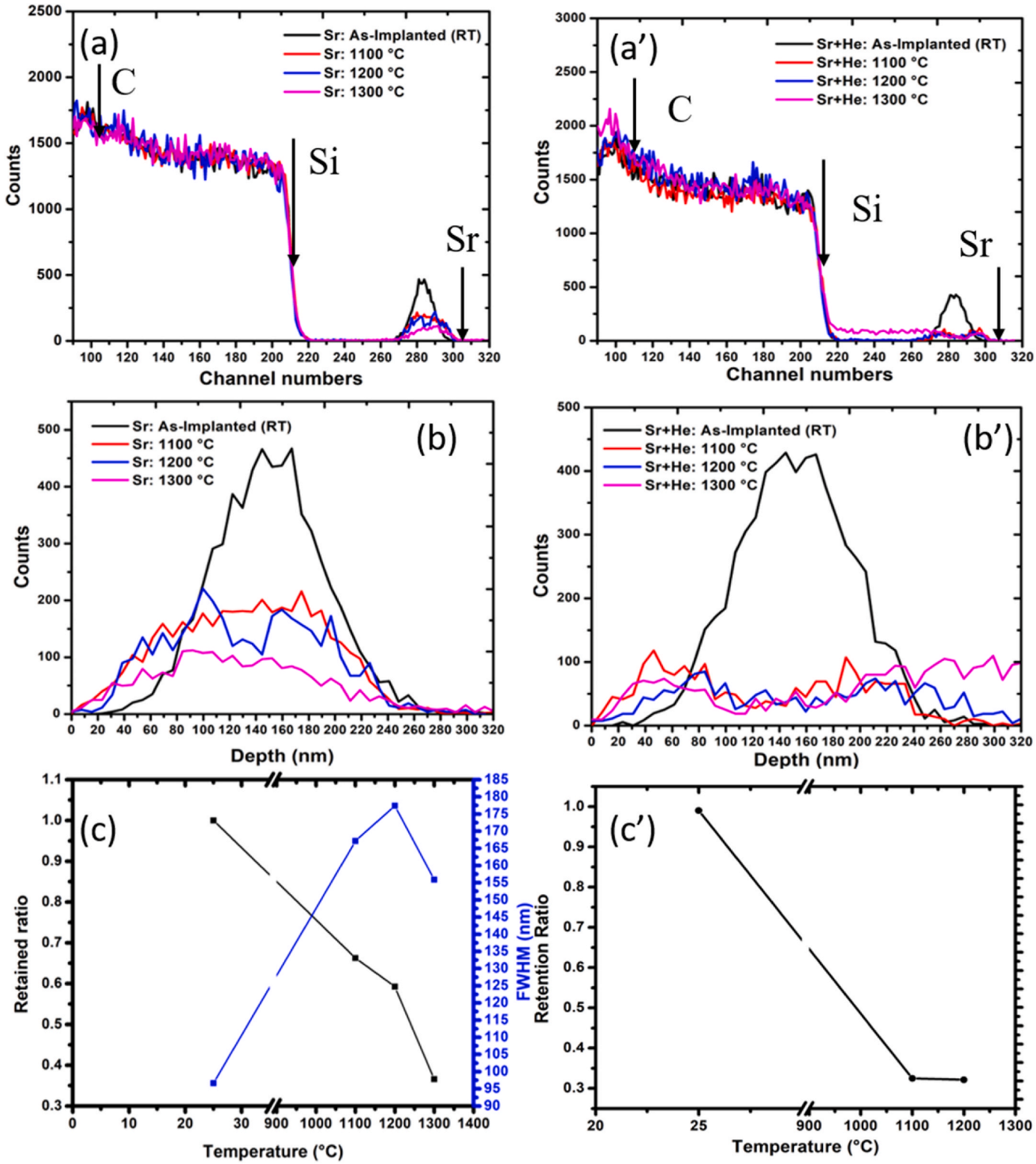

Fig. 2. RBS spectra of (a) Sr-SiC and (a') Sr + He-SiC samples, Sr depth profiles of (b) Sr-SiC samples and (b') Sr + He-SiC before and after isochronal annealing at temperatures ranging from 1100 to 1300 °C for 5 h under vacuum. (c) The FWHM in nm and retained ratio of Sr in Sr-SiC and (c') retained ratio of Sr in Sr + He-SiC sample as a function of annealing temperature.

samples annealed at 1200 °C. The Sr + He-SiC sample annealed at 1200 °C exhibited similar Sr loss of approximately 70 %, indicating no additional loss in the sample annealed at 1200 °C compared to the 1100 °C annealed sample. However, the sample annealed at 1300 °C exhibited some migration towards the bulk, in addition to the segregation observed at lower annealing temperatures. This complexity rendered it impossible to calculate the retained Sr in the Sr + He-SiC sample annealed at 1300 °C. The migration of Sr towards the bulk in the Sr + He-SiC sample annealed at 1300 °C might be due to surface roughness caused by holes as reported in Ref. [23].

The Sr migration behaviour in the Sr-SiC and Sr + He-SiC samples annealed at 1100 and 1200 °C indicated that Sr migration was relatively governed by the same phenomena. However, this migration phenomenon changed in the samples annealed at 1300 °C. To gain more insight into these different phenomena, Sr-SiC and Sr + He-SiC samples annealed at 1200 and 1300 °C were further characterized by dark-field (DF) STEM, HAADF-STEM, and EDS.

Fig. 3 shows the DF STEM [(a) and (c)] and HAADF-STEM [(b) and (d)] micrographs of Sr-SiC samples annealed at 1200 and 1300 °C for 5 h together with EDS Sr-Kα depth profiles of the as-implanted Sr-SiC and annealed Sr-SiC samples (e). The diffraction patterns taken from the damaged SiC layers of the annealed samples are also shown in Fig. 3(f) and (g). The positions of damaged-crystalline SiC interfaces are indicated by the white dashed lines in DF STEM images and by black vertical lines on the Sr-Kα EDS profiles.

Annealing of Sr-SiC samples at 1200 and 1300 °C recrystallized the initially amorphous SiC into randomly oriented nano-crystallites of different sizes, as indicated by small areas of varying contrast in the DF-STEM micrographs and diffraction patterns consisting of individual rings of multipoint diffractions from nano-crystalline SiC in Fig. 3(f) and (g). This was accompanied by a reduction of the damaged layer from 270 nm in the as-implanted Sr-SiC to 250 and 160 nm in the Sr-SiC samples annealed at 1200 and 1300 °C respectively, indicating epitaxial growth from the a-c interface.

In HAADF-STEM micrographs, regions enriched with heavy elements in a matrix of light elements appear bright, whereas the cavities in a compositionally homogeneous matrix appear dark. Hence in Fig. 3 (b) and (d), the darker and brighter structures indicate the cavities and Sr-rich areas, respectively. The EDS depth profiles of Sr-Kα in Fig. 3(e) and Sr EDS maps in the supplementary data-Fig. S1(note the background in

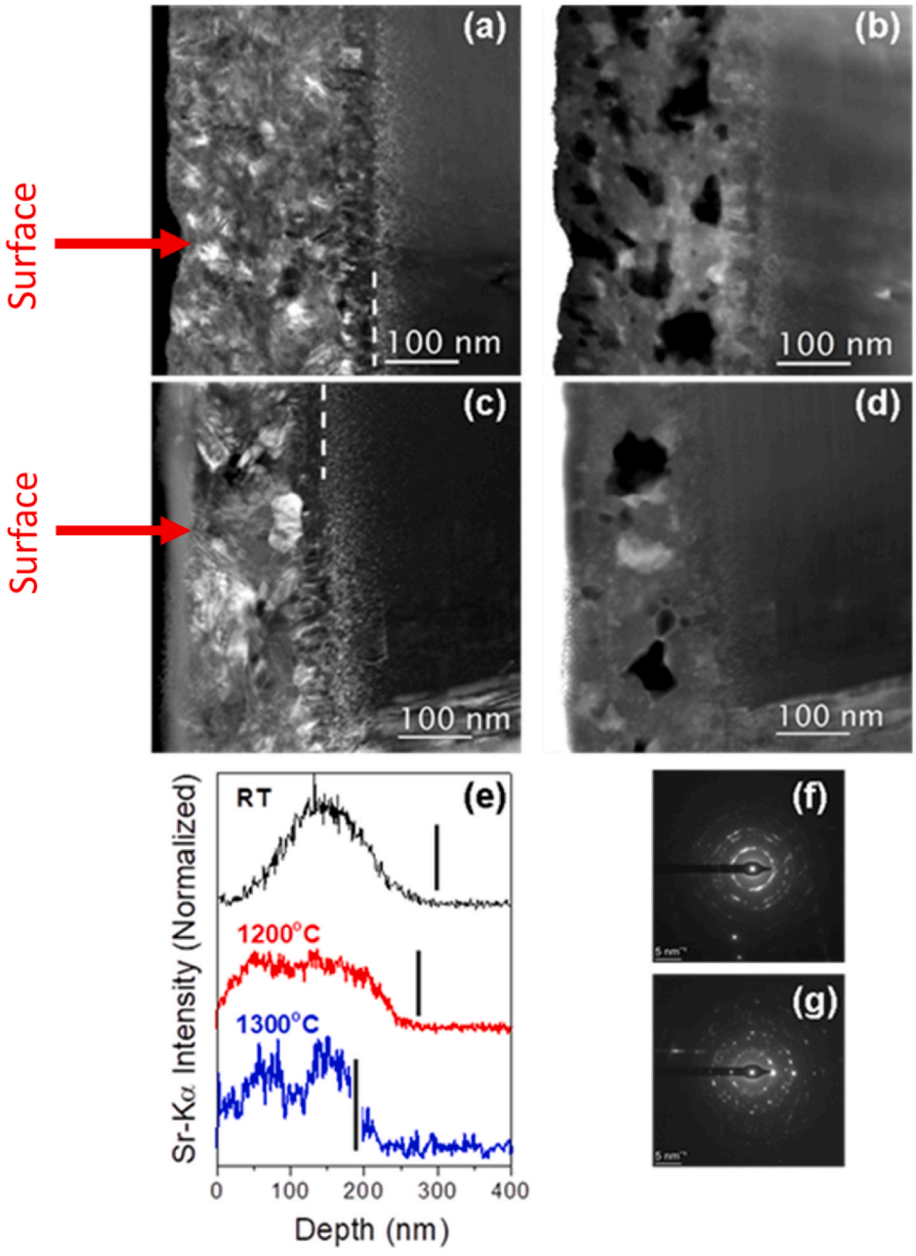

Fig. 3. Cross-sectional DFSTEM micrographs of Sr-SiC samples annealed at 1200 °C (a) and (c) 1300 °C together with their respective HAADF STEM micrographs (b) and (d). Average EDS Sr-Kα depth profiles of as implanted Sr-SiC (black), Sr-SiC after annealing at 1200 (red) and 1300 °C (blue) (e). SAD patterns (f) and (g) taken from damaged layers of Sr–SiC annealed at 1200 and 1300 °C respectively. The damaged–crystalline SiC interface positions are indicated by the white dash lines in STEM images (a) and (c) or by black vertical lines in the Sr-Kαprofiles (e).

the protective layer is due to the overlapping of platinium (Pt) and Sr X-rays.) further confirm that the brighter structures observed in Fig. 3(b) and (d) are the Sr precipitates within the nano-crystalline SiC matrix. It should be noted, however, that either the observed Sr precipitates do not yet have a crystalline structure, as no diffraction patterns (Fig. 3 (f) and (g) from crystalline Sr were identified or the small size and distribution of the Sr precipitates within the SiC matrix makes the SAD patterns challenging to interpret and confirm the structure of Sr. The latter is due to the out diffusion of implanted Sr as observed by RBS. Thus, the recrystallization of amorphous SiC with Sr implants is accompanied by the segregation of implanted Sr and the formation of cavities of different sizes. The observed cavities in the 1200 °C annealed sample are randomly distributed, with larger ones around the projected range, while most precipitates are located before and beyond the projected range. These observations align with the double-peaked Sr RBS profile observed in the Sr-SiC annealed at 1200 °C. Similarly, annealing at 1300 °C resulted in larger but fewer precipitates and cavities. Moreover, the larger precipitates appear to be closer to the surface and the interface-Fig. S1. These results correlate with the RBS results, where additional loss resulting in the Sr profile closer to the surface was observed. Annealing the Sr-SiC sample at 1300 °C resulted in the appearance of larger precipitates and cavities at the expense of smaller ones, indicating the migration and coalescence of Sr.

Amorphization induces swelling in SiC, leading to a reduction in density from 3.21 gcm^{-3} in crystalline SiC to approximately 2.75 gcm^{-3} in amorphous SiC [30,31]. Consequently, the structure retains

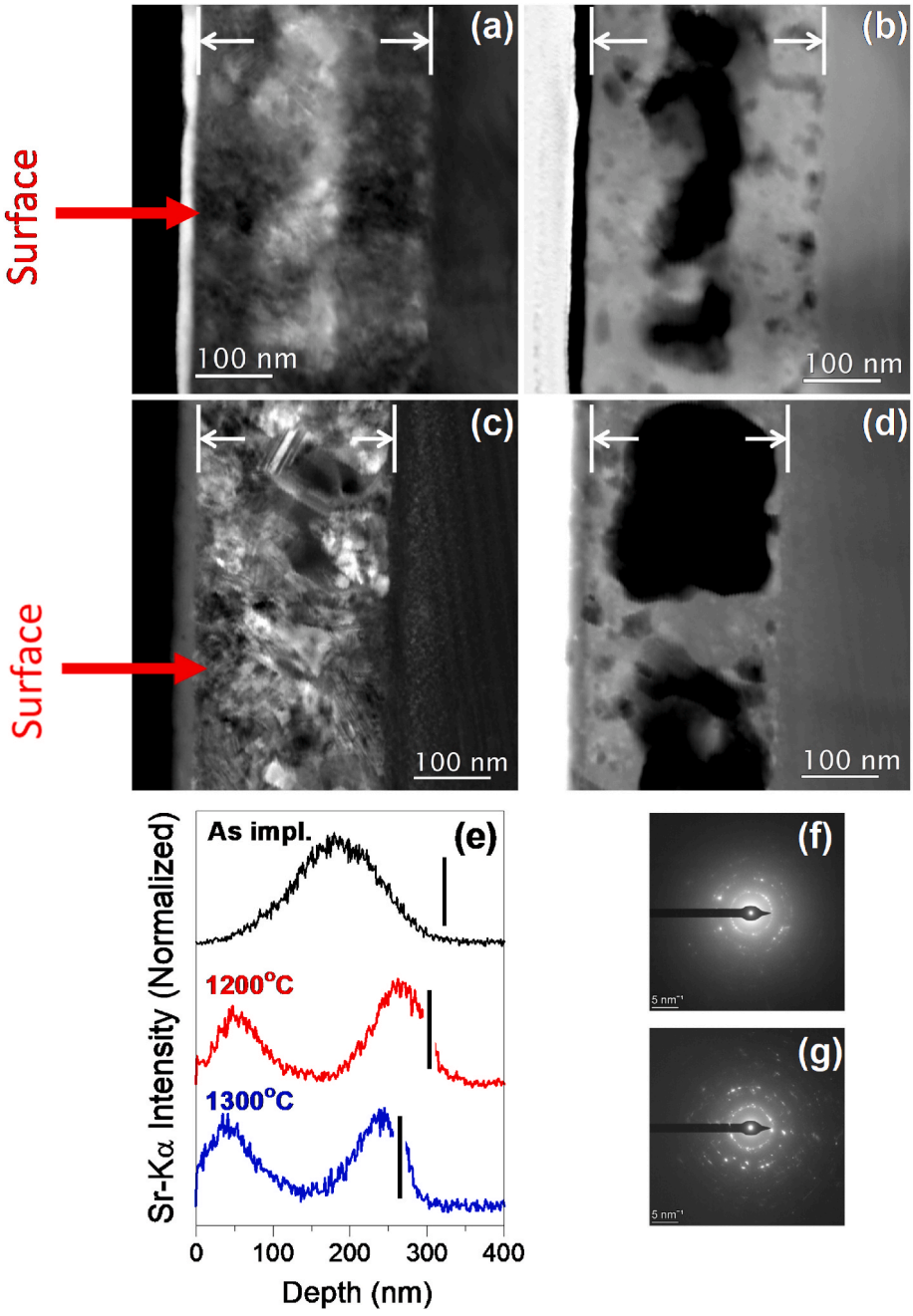

Fig. 4. Cross-sectional DF STEM micrographs of Sr + He-SiC samples annealed at 1200 °C (a) and (c) 1300 °C, their respective HAADF STEM (b) and (d). Average EDS Sr-Kα depth profiles of as implanted Sr + He-SiC (black), Sr-SiC annealed at annealing at 1200 and 1300 °C (e). SAD patterns (f) and (g) taken from damaged layers of Sr –SiC annealed at 1200 and 1300 °C respectively. The damaged–crystalline interface positions are indicated by the white dash lines in STEM images (a) and (c) or by black vertical lines in the profile plots (e).

significant strain after recrystallization due to the substantial volume change. This strain can be alleviated through the formation and propagation of cracks in the structure post-annealing, or compensatory cavities may develop to offset the volume shrinkage, as reported in the case of Ge implanted into 6H-SiC at room temperature after annealing at elevated temperatures [31]. Annealing temperatures of 1200 and 1300 °C surpass the melting point of Sr (777 °C) and approach the upper limit of the recrystallization temperature range of amorphous SiC (900–1450 °C) [32,33]. Consequently, the Sr precipitates form after the recrystallization of the SiC structure [31], effectively reducing the loss of Sr.

Fig. 4 shows the DF STEM and HAADF-STEM micrographs of Sr + He-SiC samples isochronally annealed at 1200 and 1300 °C for 5 h. Additionally, EDS Sr-Kα depth profiles of the as-implanted Sr + He-SiC annealed Sr + He-SiC samples are also presented in Fig. 4, with diffraction patterns taken from the damaged SiC layers of the annealed samples. Similar to the Sr-SC samples annealed at 1200 and 1300 °C, annealing of the Sr + He-SiC samples at these temperatures resulted in the recrystallization of the initially amorphous SiC layer. This process led to the formation of randomly oriented nano-crystallites of different sizes as shown in Fig. 4(a)–(c), (f) and (g), accompanied by epitaxial recrystallization from the a-c interface. Moreover, the annealed samples reveal He-induced defects, characterized by the dark structures in the HAADF-STEM micrographs. Larger and irregular He-induced defects are observed at the projected range, while smaller, more spherical He defects are found near the surface and at the a-c interface. Typically, He-bubbles exhibit a spherical and small morphology, whereas cavities are larger and polygon-shaped [34]. Thus, the larger structures at the projected range are identified as cavities, while the smaller ones are He-bubbles. Recrystallization occurs near the surface (of the amorphous layer) and from the amorphous-crystalline interface. The size of helium-induced defects also influences the size of the damaged region. Due to epitaxial recrystallization in the 1200 °C annealed sample, the damaged layer reduces to about 303 nm in thickness and slightly decreases to about 265 nm in the 1300 °C annealed sample.

The EDS Sr-Kα profiles of the annealed Sr + He-SiC samples are bimodal with one peak closer to the surface or before the projected range and the second beyond the projected range indicating the formation of Sr precipitates in these regions. Additionally, fewer precipitates are observed in the region with larger cavities as was confirmed by the Sr EDS maps in Fig. S2. These findings correlate with the RBS Sr profiles in Fig. 2 [(a') and (b')] and Fig. 4 (e). Hence, most cavities around the projected range contain less Sr. The increase in the size of cavities in the sample annealed at 1300 °C accompanied by the migration of Sr towards the bulk observed in the RBS results was not observed in the EDS Sr depth profiles in Fig. 4 (e). This discrepancy in the RBS and EDS Sr depth profiles of the Sr + He-SiC sample annealed at 1300 °C indicates the effect of surface roughness in the RBS as speculated earlier.

4. Discussion

Implantation of Sr at RT retained an amorphous layer in the Sr-SiC samples while co-implantation of He in the Sr-SiC resulted in the formation of nano-bubbles within the amorphous layer in the Sr + He-SiC samples. The formation of nano-He bubbles resulted in additional swelling of the amorphous layer. This phenomenon was anticipated, as the higher defect density in amorphous SiC provides more nucleation sites, thereby promoting the formation of He bubbles compared to SiC with less defects [17,35].

During annealing, the defect concentration, local strain and stresses are reduced, activating the recrystallization within the amorphous layer of the Sr-SiC samples into randomly orientated nano-crystalline SiC with cavities. This annealing process also led to a reduction in the width of the amorphous layers from the amorphous-crystalline interfaces. In contrast, in the Sr + He-SiC samples, similar recrystallization as observed in the Sr-SiC annealed was accompanied by an increase in both the quantity and size of helium-induced defects, including He-bubbles and cavities. This increase in the size of helium-induced defects hindered the relaxation of strain and stress in the annealed Sr + He-SiC samples, thereby limiting the recovery process [23]. During annealing, the migration of defects within the amorphous layer increased, facilitating the recrystallization of the amorphous phase [22,36]. In both Sr-SiC and Sr + He-SiC structures, the recrystallization process initiates at the amorphous-crystalline (a-c) interface and proceeds epitaxially, layer by layer, towards the surface [37]. In this intricate process, Si and C atoms recombine with their vacancies from the a-c interface epitaxially, elucidating the observed Sr diffusion towards the surface in the annealed Sr-SiC samples.

The significant out-diffusion of Sr is attributed to the high diffusivity of vacancies toward the surface, a consequence of the defect recovery in the amorphous phase. Sr atoms rely on vacancies for their migration through SiC. Friedland et al. [7] also noted that Sr diffusion mechanism in SiC primarily occurs during periods of defect annealing, ceasing upon the completion of defect restructuring. Specifically, Sr binds to defect complexes, is then released during their annihilation, and subsequently re-trapped by more stable defects.

The cavities observed in Sr-SiC samples following annealing at 1200 and 1300 °C seemingly have no discernible effect on the recrystallization of SiC, as confirmed by Raman spectroscopy [23]. However, their presence may influence the diffusion of Sr, especially if formed in the near-surface regions, where the exposed surface could potentially lead to Sr evaporation.

In the Sr + He-SiC samples, the presence of He-induced cavities in the damaged region hinders the recrystallization growth. A similar observation was reported by Zhang et al. [34] for He-implanted SiC. The anticipated slower recrystallization growth is compounded when cavities are present in the damaged region, and this effect intensifies with an increase in cavity size.

Zhang et al. [12] highlighted that in helium-implanted SiC, vacancy clusters act as the main traps for helium. Upon implantation, larger helium-vacancy complexes, including small bubbles, are formed (Fig. 1 (b)). Subsequent annealing results in the dissociation of He-vacancy complexes, leading to the release of helium. He-atoms closer to the surface diffuse out and are lost, while those deeper into the structure are released by unstable complexes and subsequently re-trapped by more stable complexes. This de-trapping process may also contribute to the formation of He-cavities. Consequently, competition arises between recrystallization from C and Si vacancies and the trapping and de-trapping processes involving He-vacancy complexes, contributing to the observed slow recrystallization in the Sr + He-SiC samples.

The presence of cavities establishes two distinct diffusivity paths for defects: one leading toward the free surface and the other from the a-c interface toward the cavities. The Sr distribution mirrors this behaviour, with Sr trapped both in front of and behind the cavities. This migration behaviour is due to He out-diffusion during annealing, which leaves behind empty cavities, some of which are still filled with helium. The empty cavities are responsible for capturing strontium, thereby forming precipitates, Similar trapping phenomena were observed for Fe and He co-implanted in SiC annealed at 1500 °C for 2 h [22,24,25] and for Ag and He co-implanted in SiC at room temperature then annealed at 1100 °C for 5 h [21].

As demonstrated in our previous work [23], annealing Sr + He-SiC samples at temperatures ranging from 1000 to 1300 °C in increments of 100 °C resulted in the formation of exfoliated blisters (craters) on the surface. Notably, both the size and number of these blisters increased with temperature. The emergence of surface blisters and craters is intricately linked to the formation of microcracks within the sample. With elevated temperatures, thermal stress intensifies, leading to the initiation and propagation of microcracks, ultimately culminating in the exfoliation of the surface. Consequently, the out-diffusion of Sr likely occurs through both the surface craters and microcracks, providing a rationale for the observed substantial Sr loss in the Sr + He-SiC

samples-Fig. S2. The diffusion towards the undamaged bulk in the Sr + He-SiC annealed at 1300 °C may be attributed to straggling effects, resulting from increased surface roughness due to crater formation. This broadens the backscattering spectrum, making it challenging to precisely determine the depth.

5. Conclusions

In this study, the role of annealing temperature on the migration behaviour of strontium co-implanted with helium into SiC at room temperature was investigated. Some of the Sr implanted SiC samples were implanted with He ions to the same depth. Both the Sr implanted and co-implanted SiC were isochronally annealed at 1100, 1200 and 1300 °C for 5 h. Sr implantation caused SiC to become amorphous while co-implantation of He led to the formation of nano-He bubbles in the amorphous SiC layer. Annealing resulted in the epitaxial recrystallization from the a-c interface and the formation of randomly orientated nano-crystalline SiC and some cavities in the annealed Sr-SiC samples. This was accompanied by the migration of Sr in the Sr-SiC annealed samples which was driven by the defect recovery processes in the amorphous phase, which led to significant diffusion towards the surface and formation of Sr precipitates. In the co-implanted samples, the formation of larger He-induced cavities created a barrier for epitaxial recrystallization growth, which presented trapping sites for Sr migration in front and behind the He-cavities. However, this did not inhibit the exo-diffusion of Sr, which was instead enhanced through the formation of craters and microcracks, resulting in high Sr loss in the co-implanted samples. These findings provide insights into the mechanisms underlying Sr migration in SiC, and may have implications for the safety improvement of modern fission nuclear fuel structures.

CRediT authorship contribution statement

T.T. Hlatshwayo: Writing – review & editing, Writing – original draft, Supervision, Investigation, Formal analysis, Conceptualization. **T. F. Mokgadi:** Writing – original draft, Investigation. **A. Sohatsky:** Investigation, Investigation. **Z.A.Y. Abdalla:** Writing – review & editing. **V.A. Skuratov:** Resources, Conceptualization. **E.G. Njoroge:** Writing – review & editing. **M. Mlambo:** Writing – review & editing.

Declaration of competing interest

The authors declare that they have no known competing financial interests or personal relationships that could have appeared to influence the work reported in this paper.

Data availability

Data will be made available on request.

Acknowledgements

Financial support by the National Research Foundation of South Africa (grant numbers 303088141and 2204072593) is gratefully acknowledged. This work was also supported by the Ministry of Science and Higher Education of the Russian Federation-contract 075-15-2021-709, unique identifier of the project RF-2296.61321X0037 (equipment maintenance). The Authors would also like to thank Dr M Madhuku and the technical staff at the iThemba LABS TAMS facilities, Johannesburg, South Africa for the RBS measurements.

Appendix A. Supplementary data

Supplementary data to this article can be found online at https://doi.org/10.1016/j.vacuum.2024.113676.

References

[1] Y. Katoh, L.L. Snead, I. Szlufarska, W.J. Weber, Radiation effects in SiC for nuclear structural applications, Curr. Opin. Solid State Mater. Sci. 16 (3) (2012) 143–152, https://doi.org/10.1016/j.cossms.2012.03.005.
[2] N.G. Van der Berg, J.B. Malherbe, A.J. Botha, E. Friedland, SEM analysis of the microstructure of the layers in triple-coated isotropic (TRISO) particles, Surf. Interface Anal. 42 (6-7) (2010) 1156–1159, https://doi.org/10.1002/sia.3266.
[3] INTERNATIONAL ATOMIC ENERGY AGENCY, Fuel Performance and Fission Product Behaviour in Gas-Cooled Reactors, IAEA-TECDOC-978, IAEA, Vienna, 1997. Available from: http://www-pub.iaea.org/books/IAEABooks/5633/Fuel-Performance-and-Fission-ProductBehaviour-in-GasCooled-Reactors.
[4] J.B. Malherbe, Diffusion of fission products and radiation damage in SiC, J. Phys. D 46 (47) (2013) 473001, https://doi.org/10.1088/0022-3727/46/47/473001.
[5] S. Dwaraknath, G.S. Was, Development of a multi-layer diffusion couple to study fission product transport in β-SiC, J. Nucl. Mater. 444 (1–3) (2014) 170–174, https://doi.org/10.1016/j.jnucmat.2013.09.040.
[6] S.S. Dwaraknath, G.S. Was, The diffusion of cesium, strontium, and europium in silicon carbide, J. Nucl. Mater. 476 (2016) 155–167, https://doi.org/10.1016/j.jnucmat.2016.04.034.
[7] E. Friedland, N.G. van der Berg, J.B. Malherbe, E. Wendler, W. Wesch, Influence of radiation damage on strontium and iodine diffusion in silicon carbide, J. Nucl. Mater. 425 (1–3) (2012) 205–210, https://doi.org/10.1016/j.jnucmat.2011.10.032.
[8] E. Friedland, T. Hlatshwayo, N. Van der Berg, Influence of radiation damage on diffusion of fission products in silicon carbide, Phys. Status Solidi C 10 (2) (2013) 208–215, https://doi.org/10.1002/pssc.201200457.
[9] H.A.A. Abdelbagi, V.A. Skuratov, S.V. Motloung, E.G. Njoroge, M. Mlambo, T. T. Hlatshwayo, J.B. Malherbe, Effect of swift heavy ions irradiation on the migration behavior of strontium implanted into polycrystalline SiC, Nucl. Instrum. Methods B 451 (2019) 113–121, https://doi.org/10.1016/j.nimb.2019.05.039.
[10] T.T. Hlatshwayo, N. Mtshonisi, E.G. Njoroge, M. Mlambo, M. Msimanga, V. A. Skuratov, J.B. Malherbe, S.V. Motloung, Effects of Ag and Sr dual ions implanted into SiC, Nucl. Instrum. Methods Phys. Res. B. 472 (2020) 7–13, https://doi.org/10.1016/j.nimb.2020.03.035.
[11] M.R. Gilbert, J.C. Sublet, Neutron-induced transmutation effects in W and W-alloys in a fusion environment, Nucl. Fusion 51 (4) (2011) 043005, https://doi.org/10.1088/0029-5515/51/4/043005.
[12] C.H. Zhang, S.E. Donnelly, V.M. Vishnyakov, J.H. Evans, Dose dependence of formation of nanoscale cavities in helium-implanted 4H–SiC, J. Appl. Phys. 94 (9) (2003) 6017–6022, https://doi.org/10.1063/1.1611630.
[13] B.S. Li, C.H. Zhang, H.H. Zhang, T. Shibayama, Y.T. Yang, Study of the damage produced in 6H-SiC by He irradiation, Vacuum 86 (4) (2011) 452–456, https://doi.org/10.1016/j.vacuum.2011.09.011.
[14] W. Han, B. Li, Microstructural defects in He-irradiated polycrystalline α-SiC at 1000° C, J. Nucl. Mater. 504 (2018) 161–165, https://doi.org/10.1016/j.jnucmat.2018.03.038.
[15] N. Daghbouj, B.S. Li, M. Callisti, H.S. Sen, M. Karlik, T.J.A.M. Polcar, Microstructural evolution of helium-irradiated 6H–SiC subjected to different irradiation conditions and annealing temperatures: a multiple characterization study, Acta Mater. 181 (2019) 160–172, https://doi.org/10.1016/j.actamat.2019.09.027.
[16] B. Li, H. Liu, T. Shen, L. Xu, J. Wang, F. Zhao, D. Peng, J. Li, Y. Sheng, A. Xiong, Irradiation-induced microstructure damage in He-irradiated 3C-SiC at 1000°C, J. Eur. Ceram. Soc. 40 (4) (2020) 1014–1022, https://doi.org/10.1016/j.jeurceramsoc.2019.11.026.
[17] N. Daghbouj, B.S. Li, M. Callisti, H.S. Sen, J. Lin, X. Ou, M. Karlik, T. Polcar, The structural evolution of light-ion implanted 6H-SiC single crystal: comparison of the effect of helium and hydrogen, Acta Mater. 188 (2020) 609–622, https://doi.org/10.1016/j.actamat.2020.02.046.
[18] E. Aradi, J. Lewis-Fell, G. Greaves, S.E. Donnelly, J.A. Hinks, In situ TEM investigations of the microstructural changes and radiation tolerance in SiC nanowhiskers irradiated with He ions at high temperatures, Acta Mater. 210 (2021) 116820, https://doi.org/10.1016/j.actamat.2021.116820.
[19] M. Liu, Y. Yan, Z. Zhu, R. Liu, L. Ye, H. Zhou, H. Huang, H. Microstructural evolution, swelling and hardening of CVD-SiC induced by He ions irradiation at 650° C, Ceram. Int. 49 (2) (2023) 1880–1887, https://doi.org/10.1016/j.ceramint.2022.09.152.
[20] M. Liu, H. Gong, W. Liu, R. Liu, J. Cao, Effects of He on the recrystallization and Mg diffusion in Mg ion implanted CVD-SiC, J. Nucl. Mater. 545 (2021) 152747, https://doi.org/10.1016/j.jnucmat.2020.152747.
[21] T.T. Hlatshwayo, C.E. Maepa, M. Msimanga, M. Mlambo, E.G. Njoroge, V. A. Skuratov, S.V. Motloung, J.B. Malherbe, Helium assisted migration of silver implanted into SiC, Vacuum 183 (2021) 109865, https://doi.org/10.1016/j.vacuum.2020.109865.
[22] B.S. Li, H.S. Sen, N. Daghbouj, A.T. AlMotasem, J. Lorinčík, M. Karlik, F.F. Ge, L. Zhang, Z. Sofer, I. Elantyev, M. Callisti, Thermal behavior of iron in 6H-SiC: influence of He-induced defects, Scripta Mater. 218 (2022) 114805, https://doi.org/10.1016/j.scriptamat.2022.114805.
[23] T. Mokgadi, Z. Abdalla, H. Abdelbagi, M. Msimanga, C. Maepa, V. Skuratov, T. Hlatshwayo, Helium and strontium co-implantation into SiC at room temperature and isochronal annealing: structural evolution of SiC and migration behaviour of strontium, Mater. Chem. Phys. (2023) 126998, https://doi.org/10.1016/j.matchemphys.2022.126998.
[24] A.T. AlMotasem, J. Vesely, B.S. Li, H.S. Sen, M. Karlik, J. Loriňcík, F.F. Ge, L. Zhang, V. Krsjak h, O. Laguta, M. Callisti, T. Polcar, Microstructure evolution of

iron precipitates in (Fe, He)-irradiated 6H-SiC: a combined TEM and multiscale modelling, J. Nucl. Mater. 584 (2023) p154543, https://doi.org/10.1016/j.jnucmat.2023.154543.
[25] H.S. Sen, N. Daghbouj, B.S. Li, A.T. AlMotasem, F.F. Ge, L. Zhang, M. Callisti, T. Polcar, Interaction of Stacking Faults with point/extended defects in Fe-He irradiated 6H-SiC, Acta Mater. 256 (2023) 119129.
[26] J.F. Ziegler, J.P. Biersack, The stopping and range of ions in matter, in: D. A. Bromley (Ed.), Treatise on Heavy-Ion Science, Springer, Boston, MA, 1985, pp. 93–129, https://doi.org/10.1007/978-1-4615-8103-1_3.
[27] R. Devanathan, W.J. Weber, Displacement energy surface in 3C and 6H SiC, J. Nucl. Mater. 278 (2000) 258.
[28] T.T. Hlatshwayo, L.D. Sebitla, E.G. Njoroge, M. Mlambo, J.B. Malherbe, Annealing effects on the migration of ion-implanted cadmium in glassy carbon, Nucl. Instrum. Methods Phys. Res. B 395 (2017) 34–38, https://doi.org/10.1016/j.nimb.2017.01.086, 2017.
[29] W.J. Weber, L.M. Wang, N. Yu, The irradiation-induced crystalline-to-amorphous phase transition in α-SiC, Nucl. Instrum. Methods Phys. Res.B 116 (1–4) (1996) 322–326, https://doi.org/10.1016/0168-583X(96)00066-3.
[30] A. Höfgen, V. Heera, F. Eichhorn, W. Skorupa, Annealing and recrystallization of amorphous silicon carbide produced by ion implantation, J. Appl. Phys. 84 (9) (1998) 4769–4774, https://doi.org/10.1063/1.368801.
[31] T. Gorelik, U. Kaiser, C. Schubert, W. Wesch, U. Glatzel, Transmission electron microscopy study of Ge implanted into SiC, J. Mater. Res. 17 (2) (2002) 479–486, https://doi.org/10.1557/JMR.2002.0067.
[32] W. Wesch, Silicon carbide: synthesis and processing, Nucl. Instrum. Methods Phys. Res. B 116 (1–4) (1996) 305–321, https://doi.org/10.1016/0168-583X(96)00065-1.
[33] S. Harada, T. Motooka, Recrystallization and electrical properties of MeV P implanted 6H–SiC, J. Appl. Phys. 87 (5) (2000) 2655–2657, https://doi.org/10.1063/1.372234.
[34] T. Zhang, X. He, L. Chen, J. Li, Q. Liao, S. Xu, P. Zheng, B. Li, The effect of cavities on recrystallization growth of high-fluence He implanted-SiC, Nucl. Instrum. Methods Phys. Res. B 509 (2021) 68–72, https://doi.org/10.1016/j.nimb.2021.08.012.
[35] Zhiqiang Wang, Limin Zhang, Tamer AlMotasem Ahmed, Bingsheng Li, Tomas Polcar, Nabil Daghbouj, Exploring defect behavior in helium-irradiated single-crystal and nanocrystalline 3C-SiC at 800 oC: simulation techniques, Acta Mater. 279 (2024) 120281.
[36] W. Jiang, W.J. Weber, S. Thevuthasan, S. In situ ion channeling study of gallium disorder and gold profiles in Au-implanted GaN, J. Appl. Phys. 87 (11) (2000) 7671–7678, https://doi.org/10.1063/1.373439.
[37] N. Daghbouj, B.S. Li, M. Karlik, A.J.A.S.S. Declemy, 6H-SiC blistering efficiency as a function of the hydrogen implantation fluence, Appl. Surf. Sci. 466 (2019) 141–150, https://doi.org/10.1016/j.apsusc.2018.10.005.